Timeliness-Driven integrated Sensing, Transmission, Computing and Control for Power-Communication Coupling Smart Grid

Haijun Liao, *Member, IEEE,* Hongxu Yan, Wen Zhou, Wenxuan Che, Haodong Liu, Zhenyu Zhou, *Senior Member, IEEE,* and Shahid Mumtaz, *Senior Member, IEEE*

***Abstract*—The rapid advancement of 6G, cloud-fog computing, and internet of things (IoT) has revolutionized the control paradigm of smart grid. With the closed coupling between communication and power domains, control performance heavily relies on timely and secure sensing, transmission, and computing of grid state information. Conventional approaches which treat the four sectors as separate subsystems suffer from slow convergence and even cascading control oscillations. In this paper, we address the key research problem of sensing-transmission-computing-control integrated optimization to minimize the overall voltage deviation. A timeliness-driven integrated optimization algorithm is proposed, where proactive optimization of communication resource adaptation and power-domain control decisions is conducted based on the evolution of information timeliness loss in sensing, transmission, and computing, as well as its impact on control accuracy. Particularly, a self-penalty based cost function is developed to quantify the mismatch between communication-domain resource allocation and voltage control deviation. Moreover, a novel timeliness indicator, named age of trustworthy information (AoTI), is introduced to capture timeliness-trustworthiness performance loss on proportional-integral (PI) consensus control stability margin. Consensus weights are optimized based on AoTI to further enhance convergence speed and improve control accuracy. Simulation results demonstrate that the proposed algorithm significantly improves power-domain control stability, validating the efficiency of AoTI as a critical indicator for control information importance.**

***Index Terms*—Smart grid, power-communication coupling, information timeliness, sensing-transmission-computing-control integration, PI consensus control, resource allocation**

I. Introduction

THE rapid development of advanced information and communication technologies such as 6G, internet of things (IoT), and cloud-fog computing, has evoked a paradigm shift in smart grid. The collaborative interaction among generators, grid, controllable loads, and energy storages becomes a reality due to the real-time sensing, reliable transmission, and efficient computing of critical grid states [1]. As a result, the power domain is closely coupled with the communication domain, which imposes new challenges. On the one hand, the allocation of sensing, transmission, and computing resources in the communication domain should be intelligently optimized based on the power-domain demands, providing a highly reliable and timely data channel for power control. On the other hand, efficient and robust control optimization is also a necessity to prevent false and tampered data spreading into the power domain through communication networks, causing cascading control oscillations and failures.

The integration of sensing, transmission, computing, and control is a key technology for ensuring stable operation of power-communication coupling smart grid. The four subsystems are treated as a whole and act synergistically. In sensing, with efficient data sensing period and event triggering mechanisms, critical state changes are sensed timely while avoiding redundant communication overheads. In transmission, joint optimization of data encryption intensity and channel allocation can ensure both data trustworthiness and timeliness, especially in untrusted environments with false data injection (FDI) attacks. In computing, appropriate computing resource allocation can reduce queuing delays and improve state information timeliness. In control, control decision optimization based on highly timely and trusted data can reduce voltage deviation and improve control stability.

Proportional-integral (PI) consensus control as a distributed control approach has been widely applied in smart grid. It perfectly matches grid topology since massive generators, loads, and energy storages are deployed in a decentralized and distributed manner. In [2], Wang *et al.* proposed a decentralized voltage control algorithm based on PI-consensus control and distributed resource clustering to minimize voltage deviation. In [3], Shi *et al.* considered the impact of FDI attacks and proposed a deception attack-aware consensus voltage control method for microgrids. The partial primal-and-dual (PPD) algorithm is adopted to achieve attack detection by analyzing primary and dual variables of voltage control. However, the joint optimization of power and communication domains has been ignored in the above works.

Several studies have explored multi-sector resource allocation. For sensing-transmission integration, Hua *et al.* developed an integrated sensing and communication system

Manuscript received September 27, 2024; revised January 17, 2025; accepted February 28, 2025. Date of current version March 4, 2025. This work was supported by Beijing Natural Science Foundation under Grant Number 4254074, and the Science and Technology Project of State Grid Corporation of China under Grant Number 5700-202356629A-3-2-ZN. *(Corresponding author: Zhenyu Zhou).*

H. Liao, H. Yan, W. Zhou, W. Che, H. Liu, and Z. Zhou are with State Key Laboratory of Alternate Electrical Power System with Renewable Energy Sources (North China Electric Power University), Beijing, 102206, China. (E-mail:{haijun_liao, 120221020622, zhou_wen, wenxuan_che, 120232201345, zhenyu_zhou}@ncepu.edu.cn).

Shahid Mumtaz is with the Department of Engineering, Nottingham Trent University, NG1 4FQ Nottingham, U.K., and also with the Department of Electronic Engineering, Kyung Hee University, Yongin 17104, Gyeonggi, South Korea (e-mail: dr.shahid.mumtaz@ieee.org).

to assist target detection, where pilot sequences in channel estimation and user information in transmission are jointly utilized [4]. For transmission-computing integration, an energy-efficient satellite-aerial integrated edge computing network was developed by jointly optimizing ground user device association, multi-user multi-input and multi-output launch precoding, computing task assignment and resource allocation [5]. For sensing-transmission-computing integration, Cai *et al.* proposed a low-latency computing task offloading approach for vehicular networks by investigating the coupling among sensing, communication, and computing [6]. Actual task processing delay is minimized by jointly optimizing sub-task dispatch and service selection decisions. A low-energy, low-latency short packet transmission method was developed based on sensing-transmission-computing integration [7]. The total system energy consumption is minimized while ensuring radar sensing performance and short packet transmission constraints. However, the above studies primarily focus on communication-domain resource allocation, while the joint optimization of power and communication domains has not been thoroughly investigated. For power-communication coupling, Yu *et al.* studied the impact of communication delay and packet loss on microgrid voltage tracking, and proposed a consensus-based proportional-integral predictive control strategy to reach output voltage consensus [8]. A dynamic voltage and communication channel scheduling co-design scheme was developed by considering the impact of parameter uncertainty and communication delay on voltage control [9]. Fast coordination and voltage recovery have been achieved despite limited communication channel resources. In [10], Peng *et al.* developed an algorithm to obtain both the PI-based load frequency control gain and an upper bound on the allowed communication delay. A PI consensus control algorithm was proposed to minimize the DC bus voltage deviation and improve power sharing of storage battery by considering communication delay [11].

However, these studies mainly adopt delay as the primary performance indicator in the communication domain, which may not be fully applicable to control optimization. Communication delay primarily measures information transmission efficiency but cannot accurately reflect the information timeliness loss across the entire process of sensing, transmission, computing, and control [12], [13]. Age of information (AoI) as an effective indicator for quantifying information timeliness loss, measures the deviation between the generation time of the latest state data and the current time at the receiver [14]–[16]. In [17], Klügel *et al.* analyzed the feasibility of AoI on the optimization of networked control systems and provided an AoI estimation method, where the control performance is optimized by minimizing the age penalty function. Peak age of loop (PAoL) was constructed for quantifying the sensor-controller-actuator loop [18], based on which a block length optimization method was developed to improve loop information freshness and control performance. A new transmission scheme based on context-aware learning was proposed by considering AoI of devices [19]. Numerical results demonstrate that the awareness of state information timeliness and control precision can be enhanced by leveraging AoI to guide resource allocation optimization. However, despite the numerous advantages of AoI, its application to the complex power-communication coupling smart grid still faces several technical challenges.

First, existing literatures lack in-depth analysis of the propagation path of system state changes across communication and power domains. The separate treatment of sensing, transmission, computing, and control is no longer suitable. Second, the coupling between sensing and transmission is highly complex. For instance, reducing the sensing period enables timely capture of state changes, but it also increases data backlogs of encryption, transmission, and computing queues, thereby increasing AoI. Last but not least, traditional consensus control methods have not explored the difference and fluctuation of information timeliness and trustworthiness. AoI cannot reflect the trustworthiness of control information. The mere consideration of AoI in control optimization inevitably causes tampered data spreading into the power domain from communication networks, causing cascading control oscillations. Therefore, it is necessary to design a novel timeliness indicator that balances AoI and data security for PI consensus control.

In response to these challenges, we aim to address the key research problem of sensing-transmission-computing-control integrated optimization in complex power-communication coupling smart grid. Specifically, the formulated problem is solved in three stages, where sensing period, encryption intensity, channel allocation, decryption computing resources, and consensus weights are joint optimized to minimize the overall bus voltage deviation. Next, a cost function is constructed to account for the self-penalty term arising from sensing-transmission resource mismatch and voltage control deviation, based on which sensing and transmission resource allocation is jointly optimized. Additionally, computing resource allocation is optimized to minimize the sum AoI. Finally, a novel metric named age of trustworthy information (AoTI) is introduced to guide control optimization. It captures the intrinsic relationship among control stability margin loss, AoI and trustworthiness. Compared with delay and AoI, using AoTI for consensus control not only significantly reduces convergence time, but also achieves reliable resistance to FDI attacks. The main contributions are summarized as follows.

- Timeliness-driven sensing-transmission-computing-control integrated optimization: We establish an accurate expression of the cumulative timeliness loss across sensing, transmission, and computing, and quantify its impact on power-domain control performance. This sheds insight into the design of closed-loop, integrated optimization of both communication and power domains, which breaks the rigid paradigm of unidirectional and separate implementation of sensing, transmission, computing, and control.
- Self-penalty deep actor-critic (DAC) based sensing-transmission collaborative optimization: The propagation path of sensing and transmission demand changes caused by state transitions in the power domain is deeply explored to enable real-time capture of rapid state changes. Additionally, a self-penalty term quantifying resource-demand mismatch is leveraged to update DAC network

in closed-loop to effectively resolve the paradox between resource wastage and insufficiency.

• Computing resource allocation for optimal AoI: To prevent excessive timeliness loss from compromising control stability, a computing resource allocation problem is constructed to minimize the sum AoI. Based on the derived expression between AoI evolution and computing resource allocation, triggering moments, and queue backlog, the problem is transformed into a convex one and solved in a tractable manner.

• Consensus control based on AoTI: Compared to AoI and delay, AoTI integrates the latency of the whole chain of sensing, transmission, computing and control as well as information trustworthiness. The nonlinear impact of communication-domain information timeliness and trustworthiness on power-domain control stability margin is quantified. It provides guidance on consensus weight optimization to favor state information with high timeliness and trustworthiness, improving PI consensus convergence.

II. System Model

The proposed framework of sensing-transmission-computing-control integration for power-communication coupling smart grid, is shown in Fig. 1. It consists of three layers. The sensing layer is composed of IoT devices deployed in distributed generators (DGs), loads, and energy storages to sense real-time grid state data. In the transmission and computing layer, transmitter devices (TXs) encrypt sensed data and transmit them to neighboring devices (RXs), which decrypt and compute the received data. In the PI consensus control layer, each device interacts with neighboring devices to iteratively update the consensus variables and adjust DG output based on the decrypted state variables and bus voltage deviations.

FDI attacks severely affect consensus convergence by exploiting vulnerabilities of communication channels to inject malicious data, misleading devices into making inaccurate control decisions [20]. Although increasing data encryption intensity can effectively defend against FDI attacks, it also increases decryption delay and AoI, negatively affecting convergence performance. Therefore, we focus on how to minimize the overall voltage deviation through integrated optimization of sensing, transmission, computing, and control resources. The models of sensing, transmission, computing, and control are introduced below.

A. PI Consensus-based Secondary Control Model for Smart Grid

The PI consensus-based secondary control model for smart grid is illustrated in Fig. 1. The primary control employs traditional droop control to maintain power supply-demand balance and stabilize bus voltage. The secondary control leverages PI consensus to correct the reference voltage of the primary control and improve control precision based on coordinated voltage regulation of DGs. PI consensus allows neighboring devices to exchange not only the state variables

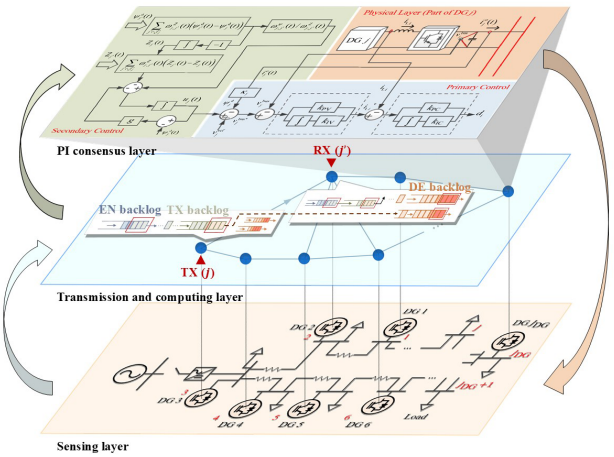

Fig. 1. The proposed framework of sensing-transmission-computing-control integration for power-communication coupling smart grid.

output by the observers but also intermediate variables that reflect the convergence performance of each device's state variables, resulting in steady state response characteristics.

Considering J devices, the buses connected to DGs are numbered as $1, \cdots, J_{\mathrm{DG}}$, while the pure load buses are numbered as $J_{\mathrm{DG}}+1, \cdots, J$. Based on Kirchhoff's current Law, the injected current at bus j is given by

$$\begin{aligned} i_j^o =& \frac{v_j^{\mathrm{bus}}}{\Omega_j^{\mathrm{load}}} + \frac{P_j^{\mathrm{load}}}{v_j^{\mathrm{bus}}} + I_j^{\mathrm{load}} \\ &+ \sum_{j' \in \mathcal{J}_j^{'}} \frac{v_j^{\mathrm{bus}} - v_{j'}^{\mathrm{bus}}}{\Omega_{j,j'}}, j = 1, 2, \cdots, J \end{aligned} \tag{1}$$

where v_j^{bus} denotes the bus voltage. $\mathcal{J}_j^{'}$ denotes the set of J' devices connected to device j. $\Omega_{j,j'}$ denotes the line impedance between j and j'. Ω_j^{load}, I_j^{load}, and P_j^{load} are the constant impedance load, current load, and power load.

The above equation can be linearized as

$$\begin{bmatrix} \Delta \boldsymbol{i_o} \\ \mathbf{0} \end{bmatrix} = \begin{bmatrix} \boldsymbol{Y}_{J_{\mathrm{DG}} \times J_{\mathrm{DG}}} & \boldsymbol{Y}_{J_{\mathrm{DG}} \times J} \\ \boldsymbol{Y}_{J \times J_{\mathrm{DG}}} & \boldsymbol{Y}_{J \times J} \end{bmatrix} \begin{bmatrix} \Delta \boldsymbol{v}^{\mathbf{bus}} \\ \Delta \boldsymbol{v}_{\boldsymbol{J}}^{\mathbf{bus}} \end{bmatrix} \tag{2}$$

where $\Delta \boldsymbol{i^o} = [\Delta i_1^o, \cdots, \Delta i_{J_{\mathrm{DG}}}^o]^T$, $\Delta \boldsymbol{v}^{\mathbf{bus}} = [\Delta v_1^{\mathrm{bus}}, \cdots, \Delta v_{J_{\mathrm{DG}}}^{\mathrm{bus}}]^T$, $\Delta \boldsymbol{v_J}^{\mathbf{bus}} = [\Delta v_{J_{\mathrm{DG}}+1}^{\mathrm{bus}}, \cdots, \Delta v_J^{\mathrm{bus}}]^T$. $\begin{bmatrix} \boldsymbol{Y}_{J_{\mathrm{DG}} \times J_{\mathrm{DG}}} & \boldsymbol{Y}_{J_{\mathrm{DG}} \times J} \\ \boldsymbol{Y}_{J \times J_{\mathrm{DG}}} & \boldsymbol{Y}_{J \times J} \end{bmatrix} \in \mathbb{R}^{J \times J}$ is the block form of the admittance matrix, with its elements expressed as

$$y_{j,j'} = \begin{cases} \sum_{j' \in \mathcal{J}_j^{'}} 1/\Omega_{j,j'} & \\ +1/\Omega_j^{\mathrm{load}} - P_j^{\mathrm{load}} \Big/ \bar{v}_j^{\mathrm{bus}^2} & \text{for } j = j' \\ -1/\Omega_{j,j'} & \text{for } j \neq j' \end{cases} \tag{3}$$

where $\bar{v}_j^{\mathrm{bus}}$ represents the grid operation voltage during linearization, which can be simplified as the rated voltage v_j^{ref}.

For DGs, the loads can be eliminated, yielding a reduced-order network equation, expressed as

$$\Delta \boldsymbol{i}^o = \boldsymbol{Y}_{J_{\mathrm{DG}}} \Delta \boldsymbol{v}^{\mathrm{bus}} \tag{4}$$

where $\boldsymbol{Y}_{J_{\rm DG}} = \boldsymbol{Y}_{J_{\rm DG}\times J_{\rm DG}} - \boldsymbol{Y}_{J_{\rm DG}\times J}\boldsymbol{Y}_{J\times J}^{-1}\boldsymbol{Y}_{J\times J_{\rm DG}}$, $\boldsymbol{Y}_{J_{\rm DG}} \in \mathbb{R}^{J_{\rm DG}\times J_{\rm DG}}$ is the reduced-order admittance matrix.

The bus voltage at device j is

$$v_j^{\rm bus}(t) = v_j^{\rm ref} - \kappa_j i_j^o(t) + u_j(t) \tag{5}$$

where κ_j is the droop coefficient, and $u_j(t)$ denotes the output control signal. Define the voltage deviation as

$$\psi_j^{\rm d}(t) = \kappa_j i_j^o(t) \tag{6}$$

The objective is to minimize the overall voltage deviation of all buses in the smart grid. The secondary control problem is formulated as

$$\begin{aligned}&\mathbf{P1}: \min_{\boldsymbol{\psi_j^{\rm d}}} f(\boldsymbol{\psi_j^{\rm d}}) = \sum_{j=1}^{J_{DG}} \frac{1}{2}(v_j^{\rm bus} - v_j^{\rm ref})^2,\\ &\text{s.t. } C_1: \psi_j^{\rm d} = \psi_{j'}^{\rm d}, \forall j, j' \in \{1, 2, \cdots, J_{\rm DG}\}\end{aligned} \tag{7}$$

where C_1 represents that the output power among the DGs must be allocated strictly in inverse proportion to the droop coefficients, that is, $\kappa_1 i_1^o(t) = \kappa_2 i_2^o(t) = \cdots = \kappa_{J_{DG}} i_{J_{DG}}^o(t)$.

When the overall voltage deviation is minimized, the deviations of the control variables u_j and the voltage deviation $\psi_j^{\rm d}$ are also minimized. Thus, $\mathbf{P1}$ can be reformulated as

$$\mathbf{P2}: \min_{\boldsymbol{\psi_j^{\rm d}}} f(\boldsymbol{\psi_j^{\rm d}}) = \sum_{j=1}^{J_{DG}} \frac{1}{2}(u_j - \psi_j^{\rm d})^2 \tag{8}$$

The optimal solution for $\mathbf{P2}$ is given by $u_j = \psi_j^{\rm d}$. Based on the PI consensus algorithm, the secondary control variables and intermediate variables are updated as

$$\begin{aligned}\dot{u}_j(t) = &\sum_{j'\in\mathcal{J}_j'} \omega_{j,j'}^{\psi}(t)\left(\psi_{j'}^{\rm d}(t) - \psi_j^{\rm d}(t)\right)\\ &- \sum_{j'\in\mathcal{J}_j'} \omega_{j,j'}^{Z}(t)\left(Z_{j'}(t) - Z_j(t)\right) + g_j(t)\nabla f(\psi_j^{\rm d}(t))\end{aligned} \tag{9}$$

$$\dot{Z}_j(t) = \sum_{j'\in\mathcal{J}_j'} \omega_{j,j'}^{Z}(t)\left(\psi_{j'}^{\rm d}(t) - \psi_j^{\rm d}(t)\right) \tag{10}$$

where $\omega_{j,j'}^{\psi}(t)$, $\omega_{j,j'}^{Z}(t)$, and $g_j(t)$ are weight coefficients. $Z_j(t)$ is an auxiliary variable that reflects the convergence of $\psi_i^{\rm d}(t)$. $\nabla f(\psi_j^{\rm d}(t))$ represents the gradient of $f(\psi_j^{\rm d}(t))$.

B. State Sensing Model based on Adjustable Sensing Period and Event Triggering

Define the sensing period variable for the IoT device of the j-th DG as $h_j(t) \in \mathcal{H}_j = \{h_j^{\min}, \cdots, h_j^{\min} + \frac{(h_j^{\max}-h_j^{\min})(n-1)}{N-1}, \cdots, h_j^{\max}\}$, where $h_j^{\min}$ and $h_j^{\max}$ represent the minimum and maximum sensing periods. The n-th sensing period is expressed as $h_j^{\min} + \dfrac{(h_j^{\max} - h_j^{\min})(n-1)}{N-1}$, with $n = 1, 2, \cdots, N$.

Then, device j performs event triggering judgment based on sensed values. If the event triggering conditions are met, device j encrypts the sensed state data and transmits them to neighboring device in set $\mathcal{J}_j^{'}$. Upon receiving the encrypted state data, the neighboring devices decrypt them and update their local states based on PI consensus. Defining the k-th event triggering moment for device j as t_j^k, the event triggering condition is given by

$$\begin{aligned}&\delta_j(t)\left\{\omega_{j,j'}^{\psi}(t)\left[e_j^{\psi}(t)\right]^2 + \omega_{j,j'}^{Z}(t)\left[e_j^{Z}(t)\right]^2\right\}\\ &\geq \sum_{j'\in\mathcal{J}_j'} \frac{(\omega_{j,j'}^{\psi}(t) + \omega_{j,j'}^{Z}(t))}{2}\left(\hat{\psi}_{j'}^{\rm d}(t) - \hat{\psi}_j^{\rm d}(t)\right)^2\end{aligned} \tag{11}$$

where $\hat{\psi}_j^{\rm d}(t) = \psi_j^{\rm d}(t_j^k)$. $\delta_j(t)$ is the event-triggered sensitivity control variable, and a lager $\delta_j(t)$ indicates higher sensitivity. $e_j^{\psi}(t)$ and $e_j^{Z}(t)$ represent the changes in the voltage deviation $\psi_j^{\rm d}$ and the auxiliary intermediate variable $Z_j(t)$ since the last event triggering, expressed as

$$e_j^{\psi}(t) = \psi_j^{\rm d}(t) - \hat{\psi}_j^{\rm d}(t) \tag{12}$$

$$e_j^{Z}(t) = Z_j(t) - \hat{Z}_j(t) \tag{13}$$

where $\hat{Z}_j(t) = Z_j(t_j^k)$.

C. Transmission and Computing Model

1) TX-Side Encryption Delay Model: After an event is triggered, device j encrypts the state sensing data. The data encryption intensity variable is defined as $w_j^k \in \mathcal{W} = \{1, \cdots, m, \cdots, M\}$, where $w_j^k = m$ represents that device j uses the m-th level of encryption intensity. The encryption complexity, security, and decryption complexity of the m-th level are denoted by $\omega_m^{\rm EN}$, ϕ_m, and $\omega_m^{\rm DE}$, respectively. The encryption delay ignoring device-side encryption queue backlog is expressed as

$$\tau_j^{k,\rm EN} = \sum_{o=1}^{M} \mathbb{1}\{w_m^k = o\}\frac{\omega_o^{\rm EN}\zeta_{{\rm EN},j}^{k,\rm ori}}{f_j} \tag{14}$$

where $\zeta_{{\rm EN},j}^{k,\rm ori}$ represents the size of state data, and f_j represents the computing resources.

Assume encryption queue backlog of device j as $Q_j^{\rm EN}(t)$. The triggering sequence number of the first packet waiting for encryption in the queue is defined as $\mathrm{HI}_{j,k-1}^{\rm EN}$. $o_j^{\rm EN}(t)$ denotes the sequence number of the last packet left the encryption queue before time t. After the k-th event triggering, if the triggering interval is less than the encryption delay $\tau_j^{\mathrm{HI}_{j,k-1}^{\rm EN},\rm EN}$ of the state data $\mathrm{HI}_{j,k-1}^{\rm EN}$, i.e., $t_j^k - t_j^{k-1} < \tau_j^{\mathrm{HI}_{j,k-1}^{\rm EN},\rm EN}$, then the encryption queue backlog increases. At this point, $o_j^{\rm EN}(t) = \mathrm{HI}_{j,k-1}^{\rm EN} - 1$. The encryption queue backlog evolves as

$$Q_j^{\rm EN}(k) = Q_j^{\rm EN}(k-1) + 1 \tag{15}$$

The encryption delay is updated as

$$\tau_j^{\tilde{k},\rm EN} = \tau_j^{\tilde{k},\rm EN} - (t_j^k - t_j^{k-1}) \tag{16}$$

where $\tilde{k} = \mathrm{HI}_{j,k-1}^{\rm EN}$.

If $t_j^k - t_j^{k-1} \geq \tau_j^{\mathrm{HI}_{j,k-1}^{\rm EN},\rm EN}$, the encryption queue backlog evolves as

$$Q_j^{\rm EN}(k) = Q_j^{\rm EN}(k-1) + 1 - \left(\arg\max_{o_j^{\rm EN}(t)}\left\{\left(t_j^k - t_j^{k-1}\right)\right.\right.$$

$$- \sum_{o=\mathrm{HI}^{\mathrm{EN}}_{j,k-1}}^{o_j^{\mathrm{EN}}(t)} \tau_j^{o,\mathrm{EN}} \geq 0 \Bigg\} - \mathrm{HI}^{\mathrm{EN}}_{j,k-1} + 1 \Bigg) \tag{17}$$

The last term represents the number of packets encrypted within the triggering interval. The encryption delay is

$$\tau_j^{\tilde{k},\mathrm{EN}} = \left[\tau_j^{\tilde{k},\mathrm{EN}} - \left(t_j^k - t_j^{k-1} - \sum_{r=\mathrm{HI}^{\mathrm{EN}}_{j,k-1}}^{\tilde{k}-1} \tau_j^{r,\mathrm{EN}} \right), 0 \right]^+ \tag{18}$$

where $\tilde{k} = \mathrm{HI}^{\mathrm{EN}}_{j,k-1} + 1, \cdots, o_j^{\mathrm{EN}}(t) + 1$.

2) TX-Side Transmission Delay Model: Assume that device j transmits the encrypted data to j'. Define the bandwidth allocation variable as $b_j(t) \in \mathcal{B}_j = \{1, 2, \cdots, c_{\max}\}$, where $c_{\max}$ represents the maximum number of channels. The transmission capacity is defined as $R_{\max}$. When $b_j(t) = c$, the transmission rate for device j is $\frac{c}{c_{\max}} R_{\max}$. The transmission delay ignoring transmission queue backlog is expressed as

$$\tau_j^{k,\mathrm{TX}} = \frac{\zeta_{\mathrm{TX},j}^{k,\mathrm{ori}} c_{\max}}{c R_{\max}} \tag{19}$$

where $\zeta_{\mathrm{TX},j}^{k,\mathrm{ori}}$ is transmission data size. Define $Q_j^{\mathrm{TX}}(t)$ as the transmission queue backlog, $\mathrm{HI}^{\mathrm{TX}}_{j,k-1}$ as the sequence number of the first packet waiting for transmission, and $o_j^{\mathrm{TX}}(t)$ as the sequence number of the last packet left the transmission queue at time t. Similar to the encryption queue backlog, if $t_j^k - t_j^{k-1}$ is less than the transmission delay $\tau_j^{\mathrm{HI}^{\mathrm{TX}}_{j,k-1},\mathrm{TX}}$, then $o_j^{\mathrm{TX}}(t) = \mathrm{HI}^{\mathrm{TX}}_{j,k-1} - 1$. The transmission queue backlog evolves as

$$Q_j^{\mathrm{TX}}(k) = Q_j^{\mathrm{TX}}(k-1) + o_j^{\mathrm{EN}}(t) - \mathrm{HI}^{\mathrm{EN}}_{j,k-1} + 1 \tag{20}$$

The transmission delay is updated as

$$\tau_j^{\hat{k},\mathrm{TX}} = \tau_j^{\hat{k},\mathrm{TX}} - (t_j^k - t_j^{k-1}) \tag{21}$$

where $\hat{k} = \mathrm{HI}^{\mathrm{TX}}_{j,k-1}$.

If $t_j^k - t_j^{k-1} \geq \tau_j^{\mathrm{HI}^{\mathrm{TX}}_{j,k-1},\mathrm{TX}}$, the transmission queue backlog evolves as

$$\begin{aligned} Q_j^{\mathrm{TX}}(k) &= Q_j^{\mathrm{TX}}(k-1) + o_j^{\mathrm{EN}}(t) - \mathrm{HI}^{\mathrm{EN}}_{j,k-1} + 1 \\ &- \Bigg(\arg\max_{o_j^{\mathrm{TX}}(t)} \Bigg\{ \left(t_j^k - t_j^{k-1}\right) - \sum_{o=\mathrm{HI}^{\mathrm{TX}}_{j,k-1}}^{o_j^{\mathrm{TX}}(t)} \tau_j^{o,\mathrm{TX}} \geq 0 \Bigg\} \\ &- \mathrm{HI}^{\mathrm{TX}}_{j,k-1} + 1 \Bigg) \end{aligned} \tag{22}$$

The transmission delay is updated as

$$\tau_j^{\hat{k},\mathrm{TX}} = \left[\tau_j^{\hat{k},\mathrm{TX}} - \left(t_j^k - t_j^{k-1} - \sum_{r=\mathrm{HI}^{\mathrm{TX}}_{j,k-1}}^{\hat{k}-1} \tau_j^{r,\mathrm{TX}} \right), 0 \right]^+ \tag{23}$$

where $\hat{k} = \mathrm{HI}^{\mathrm{TX}}_{j,k-1} + 1, \cdots, o_j^{\mathrm{TX}}(t) + 1$.

3) RX-Side Decryption Computing Delay Model: Device j' constructs independent decryption queues for encrypted data and allocates computing resources for parallel decryption and computing. For encrypted data from j, the decryption delay ignoring decryption queue backlog is expressed as

$$\tau_{j,j'}^{k,\mathrm{DE}} = \sum_{o=1}^{M} \mathbb{1}\{w_m^k = o\} \frac{\omega_o^{\mathrm{DE}} \zeta_{\mathrm{DE},j}^{k,\mathrm{ori}}}{f_{j,j'}^k} \tag{24}$$

where $\zeta_{\mathrm{DE},j}^{k,\mathrm{ori}}$ represents decrypted data size, and $f_{j,j'}^k$ indicates the computing resources allocated by device j'.

Define $Q_{j,j'}^{\mathrm{DE}}(t)$ as the decryption queue backlog, $\mathrm{HI}^{\mathrm{DE}}_{j,j',k-1}$ as the sequence number of the first packet waiting for decryption, and $o_{j,j'}^{\mathrm{DE}}(t)$ as the sequence number of packet left the decryption queue. If the triggering interval is less than the decryption delay $\tau_{j,j'}^{\mathrm{HI}^{\mathrm{DE}}_{j,k-1},\mathrm{DE}}$ of state data $\mathrm{HI}^{\mathrm{DE}}_{j,k-1}$, then $o_j^{\mathrm{DE}}(t) = \mathrm{HI}^{\mathrm{DE}}_{j,k-1} - 1$. The decryption queue backlog is

$$Q_j^{\mathrm{DE}}(k) = Q_j^{\mathrm{DE}}(k-1) + o_j^{\mathrm{TX}}(t) - \mathrm{HI}^{\mathrm{TX}}_{j,k-1} + 1 \tag{25}$$

The decryption delay is updated as

$$\tau_{j,j'}^{\ddot{k},\mathrm{DE}} = \tau_{j,j'}^{\ddot{k},\mathrm{DE}} - (t_j^k - t_j^{k-1}) \frac{f_{j,j'}^k}{f_{j,j'}^{\ddot{k}}} \tag{26}$$

where $\ddot{k} = \mathrm{HI}^{\mathrm{DE}}_{j,k-1}$.

If $(t_j^k - t_j^{k-1}) \geq \frac{f_{j,j'}^{\mathrm{HI}^{\mathrm{DE}}_{j,k-1}}}{f_{j,j'}^k} \tau_{j,j'}^{\mathrm{HI}^{\mathrm{DE}}_{j,k-1},\mathrm{DE}}$, the decryption queue backlog evolves as

$$\begin{aligned} Q_j^{\mathrm{DE}}(k) &= Q_j^{\mathrm{DE}}(k-1) + o_j^{\mathrm{TX}}(t) - \mathrm{HI}^{\mathrm{TX}}_{j,k-1} + 1 \\ &- \Bigg(\arg\max_{o_j^{\mathrm{DE}}(t)} \Bigg\{ \left(t_j^k - t_j^{k-1}\right) \\ &- \sum_{o=\mathrm{HI}^{\mathrm{DE}}_{j,k-1}}^{o_j^{\mathrm{DE}}(t)} \frac{f_{j,j'}^k}{f_{j,j'}^o} \tau_{j,j'}^{o,\mathrm{DE}} \geq 0 \Bigg\} - \mathrm{HI}^{\mathrm{DE}}_{j,k-1} + 1 \Bigg) \end{aligned} \tag{27}$$

The decryption delay is updated as

$$\tau_{j,j'}^{\ddot{k},\mathrm{DE}} = \left\{ \tau_{j,j'}^{\ddot{k},\mathrm{DE}} - \left[(t_j^k - t_j^{k-1}) - \sum_{r=\mathrm{HI}^{\mathrm{DE}}_{j,k-1}}^{\ddot{k}-1} \frac{f_{j,j'}^k}{f_{j,j'}^r} \tau_{j,j'}^{r,\mathrm{DE}} \right], 0 \right\}^+ \tag{28}$$

where $\ddot{k} = \mathrm{HI}^{\mathrm{DE}}_{j,k-1} + 1, \cdots, o_j^{\mathrm{DE}}(t) + 1$.

D. Information Timeliness Model

The AoI of device j is defined as the deviation between the generation time of the latest state data received by j and the current time t. The AoI of the state data from j' is given by

$$\mathrm{AoI}_{j,j'}^k(t) = t - t_{j'}^k \tag{29}$$

which measures the timeliness of state information from j'.

There exists a coupling relationship among information timeliness, sensing period, queue backlog, and computing resource allocation. The impact of sensing period and backlog on AoI is shown in Fig. 2(a). When a smaller sensing period is selected under small data backlog, the state data will be

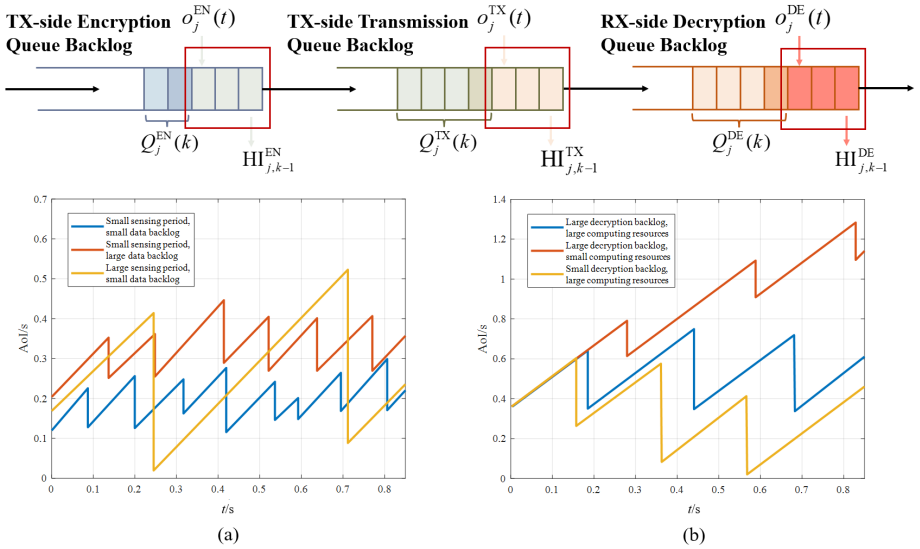

Fig. 2. The coupling relationship among information timeliness, sensing period, data backlog, and computing resource allocation: (a) The impact of sensing period and data backlog on AoI; (b) The impact of computing resource allocation on AoI.

processed quickly, keeping AoI at a low level. Conversely, choosing a larger sensing period is detrimental to timely information updating. The AoI can reach extremely low valley values due to few data backlog. On the other hand, the larger sensing period also results in higher AoI peaks due to the continuous accumulation of AoI during the large sensing interval. If a smaller sensing period is chosen under large data backlog, frequent sensing increases the queue backlogs of encryption, transmission, and computing, maintaining AoI at a higher level.

The impact of computing resource allocation and backlog on AoI is shown in Fig. 2(b). When insufficient computing resources are allocated to large decryption queue backlog, the AoI will surge due to the large queuing delay of decryption. In contrast, allocating sufficient computing resources to small backlog can reduce AoI but at the cost of computing resource wastage.

E. Control Model Considering AoI and FDI Attacks

The indicator variable for FDI attack is defined as $\Phi^k_{j,j'}$. When the attack intensity is greater than or equal to the security level, $\Phi^k_{j,j'}=1$ represents that the control information from j' received by j during the k-th event triggering cannot effectively resist FDI attack. The value of $\Phi^k_{j,j'}$ is determined as

$$\Phi^k_{j,j'}=\mathbb{1}\left\{\iota\geq\sum_{o=1}^{M}\mathbb{1}\{w^k_m=o\}\phi^{o,k}_{j,j'}\right\} \tag{30}$$

where ι represents the attack intensity, and $\phi^{o,k}_{j,j'}(t)$ denotes the security level using the o-th level of encryption intensity.

The PI consensus-based secondary control model considering AoI and FDI attacks is expressed as

$$\begin{aligned}\dot{u}_j(t)=&\sum_{j'\in\mathcal{J}_j'}\sum_{k\in\mathcal{K}_j^{j'}(t)}\omega^{\psi}_{j,j'}(t)\\&\times\left(\psi^{\mathrm{d},k}_{j'}(t-\mathrm{AoI}^k_{j,j'}(t))-\psi^{\mathrm{d}}_j(t)\right)\\&-\sum_{j'\in\mathcal{J}_j'}\sum_{k\in\mathcal{K}_j^{j'}(t)}\omega^{Z}_{j,j'}(t)\big(Z^k_{j'}(t-\mathrm{AoI}^k_{j,j'}(t))\\&-Z_j(t)+\Phi^k_{j,j'}\Delta\lambda^Z_{j,j'}\big)+g_j(t)\nabla f(\psi^{\mathrm{d}}_j(t))\end{aligned} \tag{31}$$

$$\begin{aligned}\dot{Z}_j(t)=&\sum_{j'\in\mathcal{J}_j'}\sum_{k\in\mathcal{K}_j^{j'}(t)}\omega^{Z}_{j,j'}(t)\\&\times\left(\psi^{\mathrm{d},k}_{j'}(t-\mathrm{AoI}^k_{j,j'}(t))-\psi^{\mathrm{d}}_j(t)+\Phi^k_{j,j'}\Delta\lambda^{\psi}_{j,j'}\right)\end{aligned} \tag{32}$$

where $\mathcal{K}_j^{j'}(t)$ represents the set of packet sequence numbers, and $\Delta\lambda^Z_{j,j'}$ denotes the injected false data. When $\Phi^k_{j,j'}=1$, $\Phi^k_{k,k'}\Delta\lambda^Z_{k,k'}$ and $\Phi^k_{k,k'}\Delta\lambda^{\psi}_{k,k'}$ are not equal to zero, which indicates that the secondary control variables and intermediate variables are affected by the FDI attack.

PI consensus convergence is influenced by FDI attacks and AoI. As illustrated in Fig. 3(a) and Table I, FDI attacks can reduce convergence performance and control precision and even cause control oscillations. Specifically, constant attack and step attack result in large voltage deviation and convergence time while stochastic attack leads to non-convergence. On the other hand, larger AoI also causes negative impacts, as shown in Fig. 3(b) and Table II. When AoI increases from 0.15 s to 0.35 s, the convergence time and overshoot of consensus becomes significantly larger. When AoI reaches 0.45 s, consensus iteration fails to converge. In the presence of FDI attacks, increasing encryption intensity provides better protection but also increases encryption and decryption delays, which in turn increases AoI. This demonstrates the mutual coupling between FDI attack and AoI. Therefore, the integrated design of sensing, transmission, computing and control must strike a balance between security and information timeliness.

III. Problem Formulation

We address the integrated optimization problem of sensing, transmission, computing, and control in power-communication

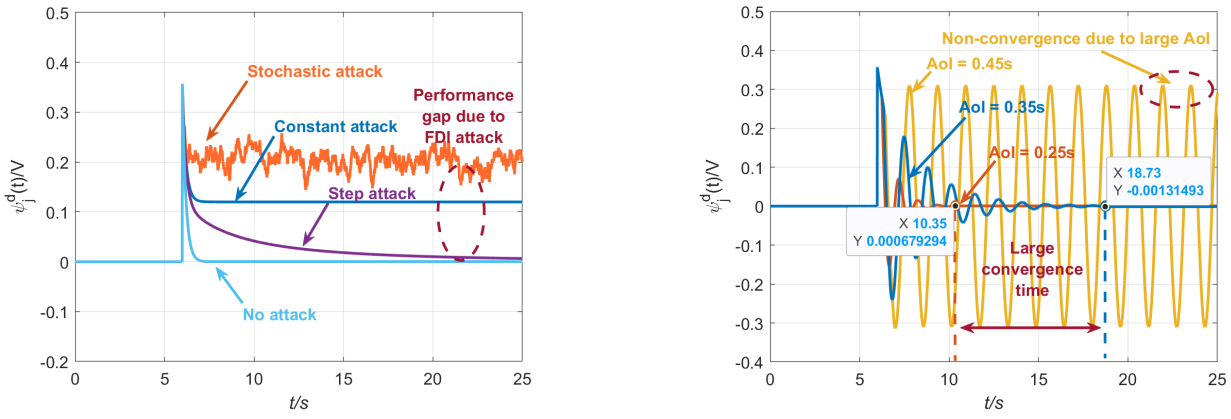

Fig. 3. The impacts of different FDI attacks and varying AoI on consensus convergence: (a) The impact of different FDI attacks; (b) The impact of varying AoI levels (5 DGs, $v^{\text{ref}} = 400$ V, $P_{\text{load}} = 5$ kW, bus-star hybrid topology).

TABLE I
IMPACT OF DIFFERENT FDI ATTACKS ON CONSENSUS CONVERGENCE.

Attack level	Convergence time /s	Overshoot of bus voltage /%	Steady-state error /V
Stochastic attack $\Delta\lambda^{Z}_{j,j'}, \Delta\lambda^{\psi}_{j,j'} = [0,1]$	Non -convergence	Non -convergence	Non -convergence
Constant attack $\Delta\lambda^{Z}_{j,j'}, \Delta\lambda^{\psi}_{j,j'} = 3$	1.32	0.03	0.12
Step attack $\Delta\lambda^{Z}_{j,j'}, \Delta\lambda^{\psi}_{j,j'} = 5 \times 10^5/t^2$	18.57	0.0624	0.016

TABLE II
IMPACT OF VARYING AOI LEVELS ON CONSENSUS CONVERGENCE.

AoI /s	Convergence time /s	Overshoot of bus voltage /%
0	1.32	0
0.15	1.37	0.0125
0.25	4.35	0.0382
0.35	12.73	0.0602
0.45	Non-convergence	Non-convergence

coupling smart grid. The optimization objective is to minimize the overall voltage deviation of all buses by jointly optimizing sensing period, encryption intensity, channel allocation, decryption computing resource allocation, and consensus weights, thereby achieving a balanced load power allocation among DGs. The optimization problem is formulated as

$$\begin{aligned}
\mathbf{MP}: &\min_{\boldsymbol{\mathcal{H}},\boldsymbol{\mathcal{W}},\boldsymbol{\mathcal{B}},\boldsymbol{\mathcal{F}},\boldsymbol{\omega}} \sum_{j=1}^{J_{\text{DG}}} \frac{1}{2}(u_j - \psi_j^{\text{d}})^2, \\
\text{s.t. } C_1: &\ \psi_j^{\text{d}} = \psi_{j'}^{\text{d}}, \forall j, j' \in \{1, 2, \cdots, J_{\text{DG}}\}, \\
C_2: &\sum_{j=1}^{J_{\text{DG}}} b_j(t) \le c_{\max}, \forall t, \\
C_3: &\sum_{j' \in \mathcal{J}_j'} f_{j,j'}^k \le f_{j,\max}^{\text{DE}}, \forall j \in \{1, 2, \cdots, J_{\text{DG}}\}, \\
C_4: &\sum_{j' \in \mathcal{J}_j'} \omega_{j,j'}^{\psi}(t) = \sum_{j' \in \mathcal{J}_j'} \omega_{j,j'}^{Z}(t) = 1, \\
&\forall j \in \{1, 2, \cdots, J_{\text{DG}}\}, \forall t
\end{aligned} \tag{33}$$

where $\boldsymbol{\mathcal{H}} = \{h_j(t)|\forall j, \forall t\}, \boldsymbol{\mathcal{W}} = \{w_j^k|\forall j, \forall k\}, \boldsymbol{\mathcal{B}} = \{b_j(t)|\forall j, \forall t\}, \boldsymbol{\mathcal{F}} = \{f_{j,j'}^k|\forall j', \forall j, \forall k\}, \boldsymbol{\omega} = \{\omega_{j,j'}^{\psi}(t), \omega_{j,j'}^{Z}(t)|\forall j', \forall j, \forall t\}$ represent the sets of optimization variables. C_1 specifies that the voltage deviation at each bus is equal and that power is strictly allocated in inverse proportion to the droop coefficient. C_2 is the bandwidth constraint, indicating that the total number of allocated channels cannot exceed $c_{\max}$. C_3 ensures that the total decryption computing resources allocated by j cannot exceed $f_{j,\max}^{\text{EN}}$. C_4 represents the weight constraints on PI consensus variables and associated intermediate variables.

IV. TIMELINESS-DRIVEN SENSING-TRANSMISSION-COMPUTING-CONTROL INTEGRATED OPTIMIZATION ALGORITHM

Traditional control methods typically treat sensing, transmission, computing, and control as independent subsystems, which are designed and optimized separately. There lacks an in-depth analysis of the propagation path of system state changes between communication and power domains. As shown in (31), the consensus convergence is influenced by factors of both communication and power domains. Therefore, it is urgent to break the rigid paradigm of sequential, unidirectional, and separate implementation of sensing, transmission, computing and control.

To address these challenges, we propose a timeliness-driven sensing-transmission-computing-control integrated optimization algorithm, as shown in Fig. 4. Within each slot, the original problem is solved in three stages. First, a self-penalty DAC-based sensing-transmission collaborative optimization algorithm is executed. By introducing a self-penalty term to quantify the mismatch between transmission demand and resource allocation, a cost function is constructed that

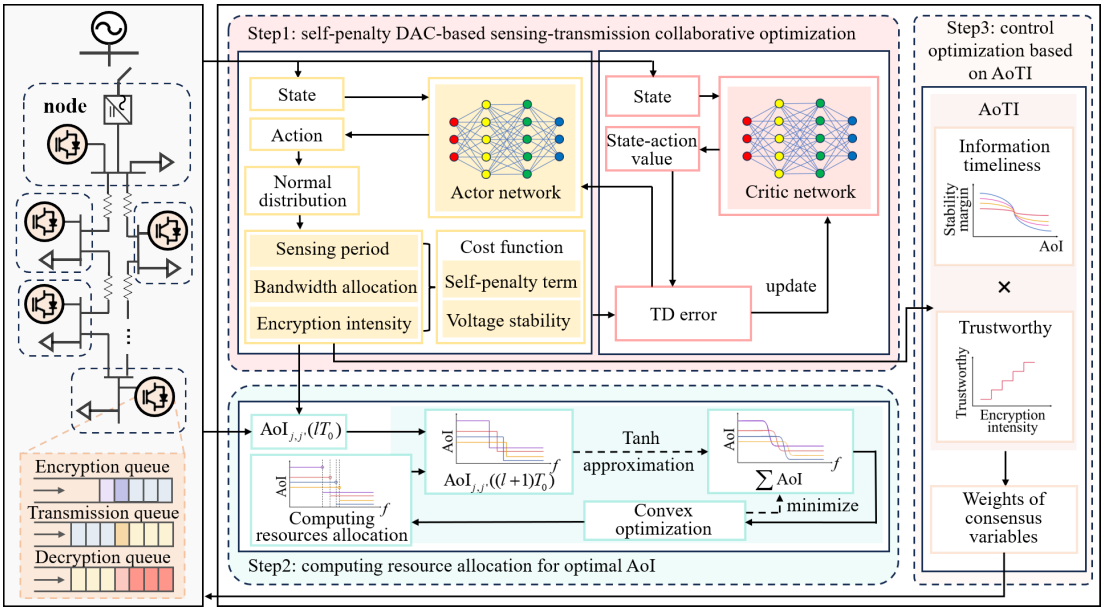

Fig. 4. The principle of the proposed timeliness-driven sensing-transmission-computing-control integrated optimization algorithm.

includes both control deviations of power domain and sensing-transmission resource adaptation deviations of communication domain. Next, a computing resource allocation algorithm for optimal AoI is proposed to minimize the total AoI of control information. Finally, a control optimization algorithm based on AoTI is introduced, which assigns higher weights to control information with high timeliness and reliability. The detailed execution flow is illustrated in Algorithm 1.

A. Self-Penalty DAC-based Sensing-Transmission Collaborative Optimization Algorithm

The joint optimization problem of sensing and transmission is formulated as

$$\mathbf{P3}: \min_{\boldsymbol{\mathcal{H}},\boldsymbol{\mathcal{W}},\boldsymbol{\mathcal{B}}} \sum_{j=1}^{J_{\mathrm{DG}}} \frac{1}{2}(u_j - \psi_j^{\mathrm{d}})^2,$$
$$\text{s.t. } C_1, C_2 \tag{34}$$

DAC is an effective method for solving **P3**. However, traditional DAC overlooks the changes of data sensing and transmission demands caused by state changes of power domain, which leads to a mismatch between transmission resource allocation and sensing-transmission demand, resulting in both resource shortage and wastage. To address this issue, a self-penalty DAC-based sensing and transmission collaborative optimization algorithm is proposed. The state space, action space, and the self-penalty based cost function are introduced as follows.

State Space: The state space of j in the l-th time slot is defined as $\mathcal{S}_j(l) = \{\mathrm{AoI}_{j,j'}^k(t), Z_{j'}(t), \psi_{j'}^{\mathrm{d}}(t) | \forall j' \in \mathcal{J'}_j, \forall k \in \mathcal{K}_j^{j'}(lT_0)\}$. Here, $\mathcal{K}_j^{j'}(lT_0)$ represents the sequence number set of decrypted data.

Action Space: The action space is defined as $\mathcal{A}_j(l) = \{\mu_j^h(l), \mu_j^b(l), \mu_j^w(l), \sigma_j^h(l), \sigma_j^b(l), \sigma_j^w(l)\}$, which represents the mean and variance variables of normal distributions of sensing period, channel allocation, and encryption intensity, i.e., $X_j^h(l)$, $X_j^b(l)$, and $X_j^w(l)$.

Self-Penalty based Cost Function: Device j constructs the self-penalty based cost function $C_j(l)$ according to the control deviation and the self-penalty term $p_j(l)$ induced by the mismatch of transmission-sensing resources, expressed as

$$C_j(l) = V\frac{1}{2} \sum_{j' \in \mathcal{J'}_j} \sum_{k \in \mathcal{K}_j^{j'}(lT_0)} \left(u_j(t - \mathrm{AoI}_{j,j'}^k(lT_0)) - \psi_j^{\mathrm{d}}(lT_0)\right)^2 + p_j(l) \tag{35}$$

where V represents the tradeoff between the power-domain control performance and the communication-domain resource adaptation. The term $p_j(l)$ will be elaborated in (37).

The proposed algorithm is implemented as four steps.

Step 1 (Initialization): Initialize the actor and critic networks $\boldsymbol{\theta}_j$ and $\boldsymbol{\xi}_j$ of device j. Initialize the number of training rounds, discount factor, learning rate of actor network δ_a, and learning rate of critic network δ_c.

Step 2 (Decision making): At slot l, the state $\mathcal{S}_j(l)$ is input into $\boldsymbol{\theta}_j$ to obtain the action $\mathcal{A}_j(l)$, and the normal distributions corresponding to sensing period, channel allocation and encryption intensity are also generated. By performing random sampling and rounding, the respective optimization results are derived. Under the channel number constraint, channel allocation action $x_j^b(l)$ is proportionally adjusted as

$$b_j(l) = \left\lfloor \frac{x_j^b(l) c_{\max}}{\sum_{j=1}^{J_{\mathrm{DG}}} x_j^b(l)} \right\rfloor \tag{36}$$

where $\lfloor \cdot \rfloor$ denotes the floor function.

Step 3 (Performance evaluation): Execute the action and transfer to the next state $\mathcal{S}_j(l+1)$. Calculate the cost function value $C_j(l)$ based on (35). The self-penalty term $p_j(l)$ is defined as the gap between the amount of data that can

Algorithm 1: Timeliness-driven sensing-transmission-computing-control integrated optimization algorithm

Input: $\mathcal{S}_j(l), \forall j' \in \mathcal{J'}_j, \forall k \in \mathcal{K}_j^{j'}(lT_0)$
Output: $\mathcal{A}_j(l)$
for $l = 1, 2, 3, \cdots$ **do**
  Self-penalty DAC-based sensing-transmission collaborative optimization:
  for $j = 1, 2, 3, \cdots$ **do**
    Load state and obtain actions based on DAC.
    Obtain $x_j^h(l)$, $x_j^b(l)$ and $x_j^w(l)$ based on random distributions $X(l)_j^h$, $X_j^b(l)$, and $X_j^w(l)$.
    Obtain channel allocation action $b_j(l)$ based on (36).
    Computing resource allocation for optimal AoI:
    Obtain AoI evolution $\text{AoI}_{j,j'}^k(T_0(l+1))$ as (40).
    Approximate $\text{AoI}_{j,j'}^k(T_0(l+1))$ as a continuous function by (42).
    Allocate computing resources $f_{j,j'}(lT_0)$ to minimize the overall AoI.
    Control optimization based on AoTI:
    Calculate $\text{AoTI}_{j,j'}^k((l+1)T_0)$ as (44).
    Determine $\omega_{j,j'}^{k,Z}(t)$ and $\omega_{j,j'}^{k,\psi}(t)$ based on $\text{AoTI}_{j,j'}^k((l+1)T_0)$ as (45).
    Calculate the self-penalty value $p_j(l)$ as (37).
    Calculate cost function $C_j(l)$ as (35).
    Transfer to the next state.
    Calculate TD error $\eta_j(l)$ as (38).
    Update DAC networks by gradient descent method.
  end
end

be transmitted and the maximum amount of data requiring transmission, i.e.,

$$p_j(l) = \left[\frac{b_j(l)}{c_{\max}} R_{\max} T_0 - \sum_{o=\text{HI}_{j,k-1}^{\text{TX}}}^{\text{HI}_{j,k-1}^{\text{TX}}+Q_j^{\text{TX}}((l-1)T_0)} \zeta_{\text{TX},j}^{o,\text{ori}}, 0\right]^+ \tag{37}$$

A larger $p_j(l)$ indicates a higher degree of mismatch of sensing-transmission resources.

Step 4 (Learning updates): Critic network calculates temporal difference (TD) error based on current state and action, i.e.,

$$\eta_j(l) = C_j(l) + \gamma_j \hat{\Lambda}_j(\mathcal{S}_j(l+1), \boldsymbol{\xi}_j) - \hat{\Lambda}_j(\mathcal{S}_j(l), \boldsymbol{\xi}_j) \tag{38}$$

where γ_j represents the discount factor, and $\hat{\Lambda}_j(\mathcal{S}_j(l), \boldsymbol{\xi}_j)$ denotes the critic network's evaluation value of the current state. The parameters of critic network are updated using the TD error as $\boldsymbol{\xi}_j \longleftarrow \boldsymbol{\xi}_j + \delta_c \eta_j(l)$. Based on the TD error and the gradient descent method [21], update the parameters of actor network as $\boldsymbol{\theta}_j \longleftarrow \boldsymbol{\theta}_j + \delta_a \eta_j(l) \bigtriangledown_\theta \pi_\theta(S_j(l), a_j(t))$.

B. Computing Resource Allocation Algorithm for Optimal AoI

The sequence number set of data received by device j from j' at slot l is denoted as $\mathcal{K}_{j,j'}^{\text{EN}}(l)$. The computing resource allocation problem is formulated as

$$\begin{aligned} \mathbf{P4}: &\min_{\boldsymbol{\mathcal{F}_j}} \sum_{j' \in \mathcal{J}_j'} \sum_{k \in \mathcal{K}_{j,j'}^{\text{EN}}(l)} \text{AoI}_{j,j'}^k(lT_0), \\ &\text{s.t. } \tilde{C}_3: \sum_{j' \in \mathcal{J}_j'} f_{j,j'}(lT_0) \le f_{j,\max}^{\text{DE}} \end{aligned} \tag{39}$$

Define the sequence number set of decrypted data as $\mathcal{K}_j^{k*}(l)$. Then, the AoI evolves as

$$\begin{aligned} \text{AoI}_{j,j'}^k(T_0(l+1)) &= \text{AoI}_{j,j'}^k(lT_0) + \mathbb{1}\{k \notin \mathcal{K}_j^{k*}(l)\} T_0 \\ &+ \mathbb{1}\{k \in \mathcal{K}_j^{k*}(l)\} \left\{ \sum_{\forall o \in \mathcal{K}_j^{k*}(l), o \le k} \tau_{j,j'}^{o,\text{DE}} \right\} \end{aligned} \tag{40}$$

where the indicator function for completed decryption can be rewritten as

$$\begin{aligned} &\mathbb{1}\{k \in \mathcal{K}_j^{k*}(l)\} \\ &\to f_{j,j'}(l) T_0 - \sum_{s=Q_{j,j'}^{\text{DE}}(T_0 l)[1]}^{k} \sum_{o=1}^{M} \mathbb{1}\{w_j^k = o\} \zeta_{\text{DE},j,j'}^o \omega_o^{\text{DE}} \\ &= X_{j,j'}^k(l) \ge 0 \end{aligned} \tag{41}$$

Additionally, we can further approximate (40) as a continuous function based on tanh function, i.e.,

$$\begin{aligned} &\text{AoI}_{j,j'}^k((l+1)T_0) = \text{AoI}_{j,j'}^k(lT_0) \\ &+ \frac{1}{2}\left[1 - \tanh\left(X_{j,j'}^k(l)\right)\right] T_0 \\ &+ \frac{1}{2}\left[1 + \tanh\left(X_{j,j'}^k(l)\right)\right] \left\{ \sum_{\forall o \in \mathcal{K}_j^{k*}(l), o \le k} \tau_{j,j'}^{o,\text{DE}} \right\} \end{aligned} \tag{42}$$

Based on (42), $\mathbf{P4}$ is transformed into a convex optimization problem, which can be solved easily.

C. Control Optimization Algorithm based on AoTI

Based on the control information obtained after decryption, the control optimization problem is formulated as

$$\begin{aligned} \mathbf{P5}: &\min_{\boldsymbol{\omega}} \sum_{j=1}^{J_{\text{DG}}} \frac{1}{2}(u_j - \psi_j^{\text{d}})^2, \\ &\text{s.t. } C_4 \end{aligned} \tag{43}$$

We propose a consensus weight optimization method based on AoTI, defined as the product of an increasing loss function of AoI regarding time and a decreasing function of trustworthiness. It can simultaneously evaluate the impacts of both information timeliness and trustworthiness on control, and provide guidance for consensus weight optimization to favor timely and trustworthy state information, which is expressed as

$$\text{AoTI}_{j,j'}^k(t) = e^{-\alpha_j e^{-\beta_j \text{AoI}_{j,j'}^k(t)}} \cdot \left(1 - \sum_{o=1}^{M} \mathbb{1}\{w_{j'}^k = o\} \phi_{j,j'}^{o,k}\right) \tag{44}$$

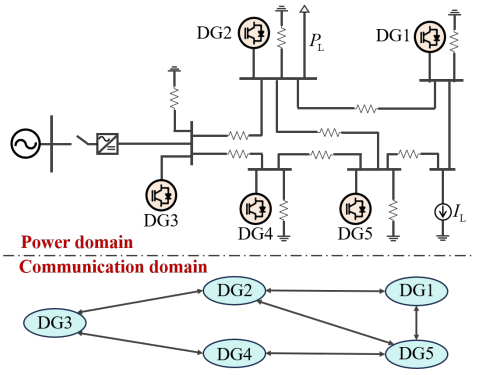

Fig. 5. Simulation topology.

where the first term employs the Gompertz function to describe the impact of AoI on control stability. α_j and β_j are used to adjust the rate of change in control stability margin loss caused by the increase of AoI.

The consensus control weight based on AoTI is defined as

$$\omega_{j,j'}^{k,Z}(t) = \omega_{j,j'}^{k,\psi}(t) = \frac{\text{AoTI}_{j,j'}^{k}((l+1)T_0)}{\sum_{j'\in\mathcal{J}_j'}\sum_{\forall k\in\mathcal{K}_j^{k*}(l)}\text{AoTI}_{j,j'}^{k}((l+1)T_0)} \quad (45)$$

As indicated by (45), control information with high timeliness and trustworthiness carries greater weight in the consensus convergence process, preventing the spread of communication-domain performance deviations into the power domain, thereby enhancing both the speed and accuracy of consensus convergence.

D. Computational Complexity

The computational complexity of the proposed algorithm consists of three parts. In the first part of self-penalty DAC-based sensing-transmission collaborative optimization, the computational complexities of initialization, decision making, performance evaluation, and learning update are $\mathcal{O}(|\boldsymbol{\theta}_j|+|\boldsymbol{\xi}_j|)$, $\mathcal{O}(|\mathcal{A}_j(l)|)$, $\mathcal{O}(1)$, and $\mathcal{O}(B\times(|\boldsymbol{\theta}_j|+|\boldsymbol{\xi}_j|))$, where $|\boldsymbol{\theta}_j|$ and $|\boldsymbol{\xi}_j|$ are the numbers of actor network parameters and critic network parameters. $|\mathcal{A}_j(l)|$ and B are the numbers of actions and training samples. The computational complexity of computing resource allocation for optimal AoI is $\mathcal{O}(J-1+\Gamma\times J^{\rho})$. Γ is the required iterations to achieve convergence, and the value of constant ρ depends on the utilized convex optimization algorithm. The computational complexity of control optimization based on AoTI is $\mathcal{O}(J-1)$. Therefore, the total complexity of the proposed algorithm is $\mathcal{O}(|\boldsymbol{\theta}_j|+|\boldsymbol{\xi}_j|+2(J-1)+\Gamma\times J^{\rho})$

TABLE III
SIMULATION PARAMETERS

Parameter	Value	Parameter	Value	Parameter	Value
Ω_j^{load}	10 Ω	$\Omega_{j,j'}$	0.01 Ω	v_j^{ref}	400V
κ_1	0.1 Ω	κ_2	0.1 Ω	κ_3	0.2 Ω
κ_4	0.2 Ω	κ_5	0.2 Ω	g_j	10
N	5	$h_j^{\min}$	10 ms	$h_j^{\max}$	50 ms
$\zeta_{\text{EN},j}^{k,\text{ori}}$	0.1 Mbit	$c_{\max}$	30	γ_j	0.99

V. Simulation Results

The simulation is implemented on three ThinkStation 7920 servers (Intel(R) Xeon(R) Gold 5118/128GB/2.5TB/P2000) and performed via MATLAB R2024b. As shown in Fig. 5, a DC microgrid system simulation environment consisting of 5 DGs is constructed based on the topology of an industrial park in China, as well as the practical operation conditions including distributed photovoltaic outputs and load fluctuations. The DC bus voltage reference is set to 400 V. Each DG includes a DC power generator, a DC/DC converter, and a passive filter, with the switching frequency of 10 kHz. The line impedance is set as 0.01 Ω, and a constant current load of I_{L} = 5 A is connected to the system. Other simulation parameters are shown in Table III [22]–[25].

The proposed algorithm has been further validated under four cases by considering the influence of load fluctuation (Case 1), grid topology variation (Case 2), communication failure (Case 3), large network size and different topologies (Case 4). In particular, its applicability in real-world microgrids with complex load profiles and load fluctuations is verified in Case 1. Its sensitivity to grid topology changes is validated in Case 2. Its robustness against communication failures is demonstrated in Case 3. Its feasibility and scalability

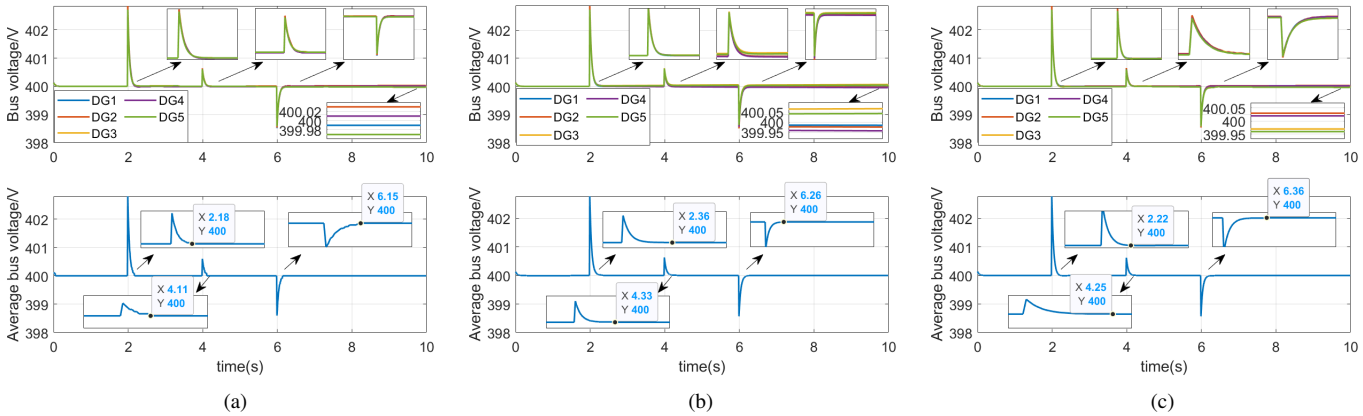

Fig. 6. Bus voltage stability performance under load fluctuation: (a) Proposed; (b) Baseline 1; (c) Baseline 2.

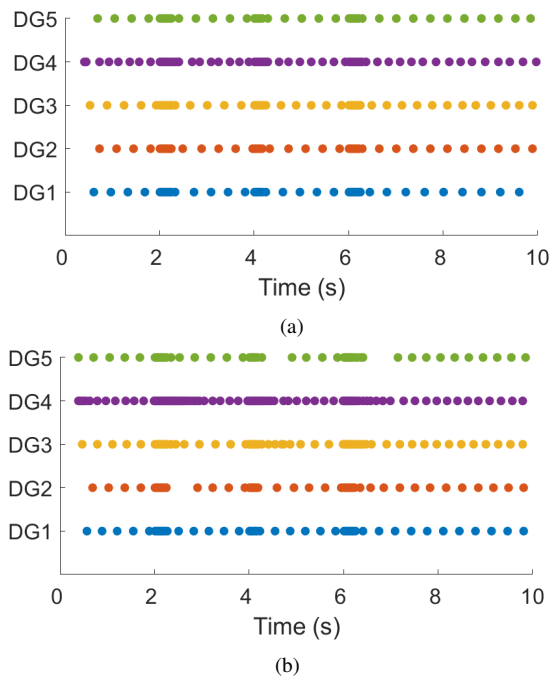

Fig. 7. Sensing event triggering moments comparison: (a) Proposed; (b) Baseline 2.

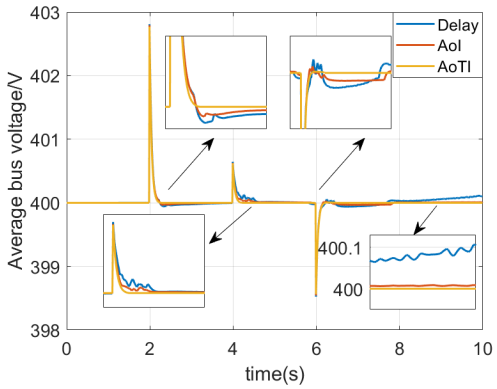

Fig. 8. Bus voltage stability performance comparison under delay, AoI, and proposed AoTI.

for large network sizes as well as different grid topologies and transmission rates are evaluated in Case 4.

Two existing works [11] and [19] are slightly modified as baseline algorithms for comparison. Baseline 1 refers to conventional consensus control based on communication delay, where both transmission and computing resources are optimized to minimize communication delay. It employs a time-triggered mechanism, i.e., state data are sensed at fixed intervals. The highest level of data encryption is adopted. Baseline 2 aims to minimize AoI based on sensing-communication-computing integrated resource allocation. The same consensus weight is adopted for all devices.

A. Case 1: Load Fluctuation

Case 1 consists of three load fluctuations. An additional 10 kW constant power load is connected to bus 2 at $t = 2$ s. The load is increased from 10 kW to 15 kW at $t = 4$ s, and is disconnected at $t = 6$ s.

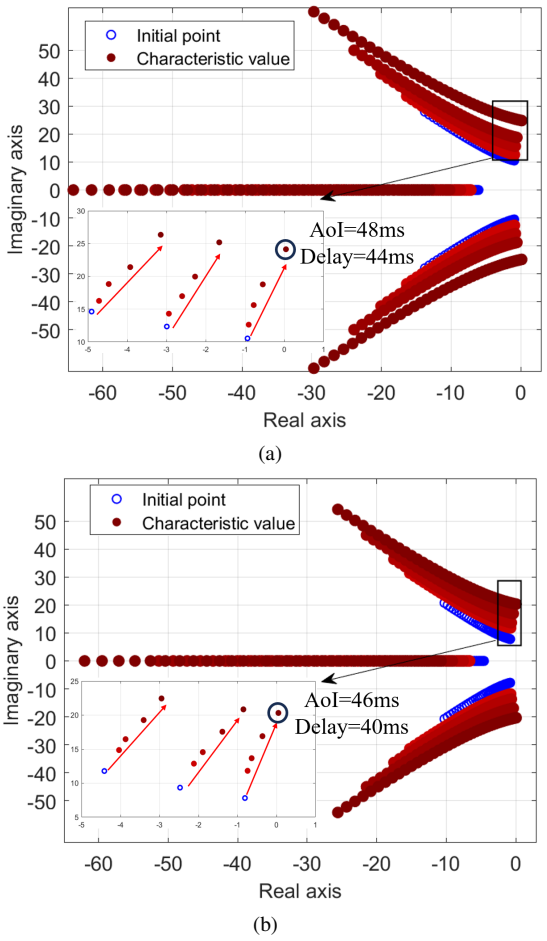

Fig. 9. Root track comparison of different communication-domain metrics: (a) AoTI; (b) Delay.

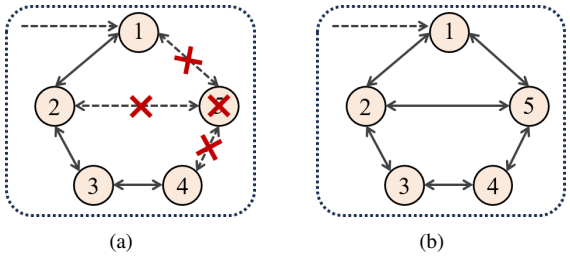

Fig. 10. Grid topology variation: (a) DG5 disconnection; (b) DG5 reconnection.

Figure 6 presents the bus voltage stability performance under load fluctuation. After consensus control, the average bus voltage of the proposed algorithm stabilizes at exactly 400 V. Compared to baseline 2, the required convergence time since load disconnection is reduced from 360 to 150 ms, and the convergence speed under three load fluctuations is increased by 46.99% due to the consideration of AoTI-based consensus weight optimization. Baseline 1 performs the worst, i.e., a total of 950 ms is required to reach voltage stability under three load fluctuations, which is 53.68% higher than the proposed algorithm. This improvement of the proposed algorithm is attributed to the abilities of timely capturing state changes and dynamically adjusting resource allocation,

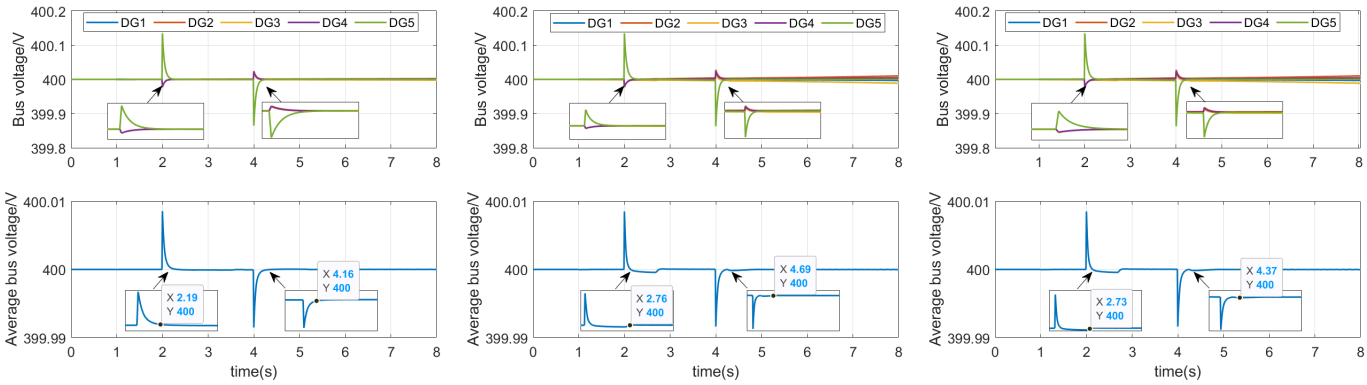

(a) (b) (c)

Fig. 11. Bus voltage stability performance under grid topology variation: (a) Proposed; (b) Baseline 1; (c) Baseline 2.

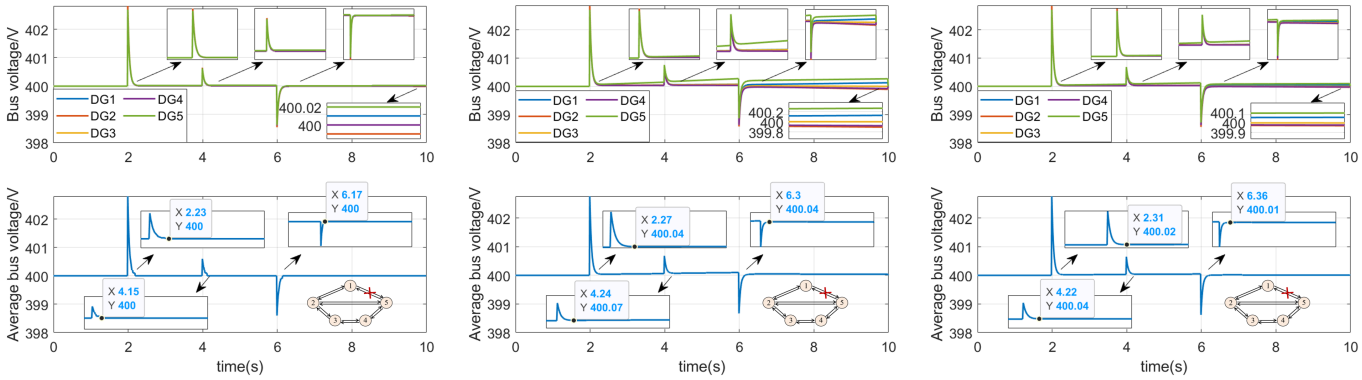

(a) (b) (c)

Fig. 12. Bus voltage stability performance under bidirectional communication failure between DG1 and DG5: (a) Proposed; (b) Baseline 1; (c) Baseline 2.

ensuring timely and reliable delivery of control information.

Figure 7 illustrates the event triggering moment comparison. Compared to baseline 2, the event triggering frequency during stable operation is decreased to alleviate data queue backlogs of encryption, transmission, and decryption. For example, the number of triggered events is reduced by 72 under stable operation. On the other hand, the frequency is significantly increased to capture state changes, which reduces AoI and accelerates consensus convergence. Specifically, the total triggering number is increased by 89 during three load fluctuations.

To further demonstrate the advantage of using AoTI for control optimization, a step FDI attack as $\Delta\lambda^{Z}_{j,j'} = 5\times10^{4}/t^{2}$ is imposed. Fig. 8 shows the bus voltage stability performance comparison under delay, AoI, and AoTI. AoTI-based consensus control achieves a reduction in convergence time by 53.96% and 36.15% compared to transmission delay-based and AoI-based approaches, respectively. Moreover, the voltage oscillations caused by FDI attacks are effectively eliminated. In comparison, using AoI without considering the trustworthiness of control information leads to non-optimal convergence, i.e., a 0.01 V voltage deviation. Transmission delay-based consensus control results in significant oscillations and even convergence failure due to the ignorance of control information timeliness loss.

Figure 9 shows the root locus of different communication-domain metrics. As AoI increases from 10 ms to 50 ms, and communication delay increases from 7 ms to 40 ms, the characteristic roots of the proposed AoTI-based control optimization algorithm and delay-based control optimization algorithm move closer to the imaginary axis. When AoI reaches 48 ms and delay reaches 44 ms, the characteristic roots of the proposed AoTI-based control optimization algorithm cross the imaginary axis, and the control becomes unstable. However, the corresponding AoI and delay when delay-based control optimization algorithm becomes unstable are 46 ms and 40 ms, respectively. This demonstrates that AoTI is a more accurate and suitable communication-domain metric to improve control stability and robustness.

B. Case 2: Grid Topology Variation

Case 2 validates the robustness against grid topology variation. As shown in Fig. 10(a), DG5 disconnects from the grid at $t = 2$ s, i.e., all of the communication links connected to DG5 are interrupted. At $t = 4$ s, DG5 reconnects to the grid as shown in Fig. 10(b).

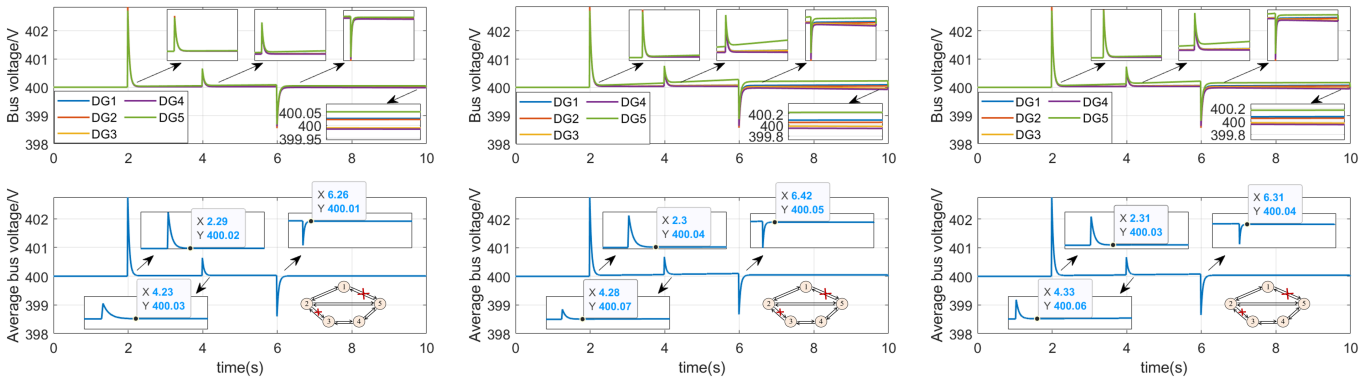

(a) (b) (c)

Fig. 13. Bus voltage stability performance under bidirectional communication failure between DG1 and DG5 and unidirectional communication failure between DG2 and DG3: (a) Proposed; (b) Baseline 1; (c) Baseline 2.

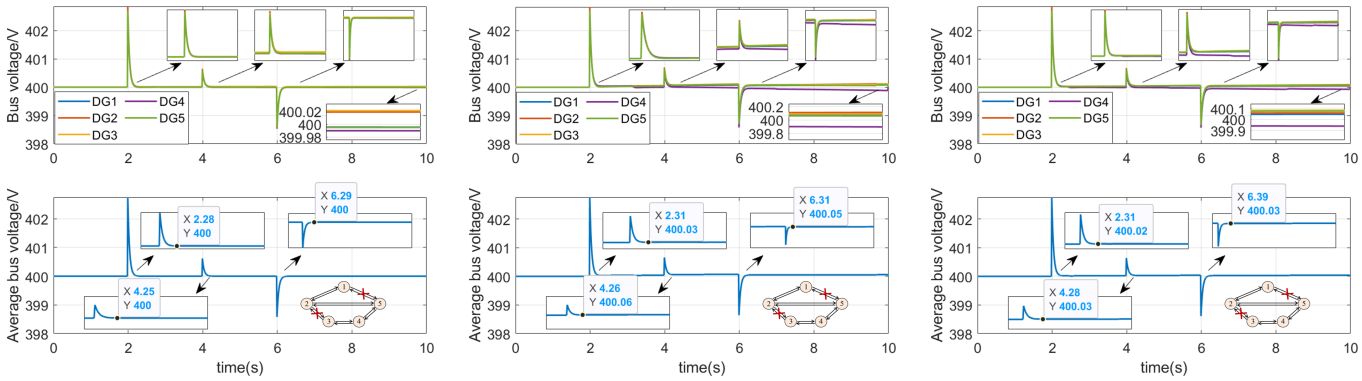

(a) (b) (c)

Fig. 14. Bus voltage stability performance under two bidirectional communication failures between DG1 and DG5 as well as DG2 and DG3: (a) Proposed; (b) Baseline 1; (c) Baseline 2.

Figure 11 shows the bus voltage stability performance under grid topology variation. After disconnection, the active power output of DG2 has to be compensated by the remaining four DGs in proportion to the droop coefficient. The required convergence time is 190 ms. Upon DG2's reconnection, the average bus voltage converges to 400 V in only 160 ms, and the operation states of 5 DGs are consistent with initial states. This verifies the robustness of the proposed algorithm against grid topology variation.

C. Case 3: Communication Failure

Figure 12 shows the bus voltage stability performance under bidirectional communication failure between DG1 and DG5. Compared to Case 1 without communication failure, all three algorithms require longer durations to reach voltage stability under the occurrence of load fluctuation. Nevertheless, the proposed algorithm exhibits the shortest convergence time, reducing it by 32.10% and 38.20% compared to the two baseline algorithms, respectively.

Figure 13 shows the bus voltage stability performance under bidirectional communication failure between DG1 and DG5 and unidirectional communication failure from DG2 to DG3. All three algorithms cannot converge to 400 V due to topology asymmetry caused by the unidirectional communication failure. Compared to baseline algorithms, the proposed algorithm results in the smallest voltage deviation, which is reduced by 62.50% and 53.85%.

Figure 14 shows the bus voltage stability performance under bidirectional communication failure between DG1 and DG5 and failure between DG2 and DG3. The topology becomes symmetric and bidirectionally connected. Under this new bus topology, all three algorithms reach stability and converge to 400 V eventually, but require a longer convergence time. Comparing Fig. 13 with Fig. 14, it is concluded that topology asymmetry is the root cause of the nonoptimal convergence. Another finding is that the proposed algorithm can rapidly stabilize bus voltage even with limited topology connectivity, which demonstrate its robustness against communication failure and scalability across various grid topologies.

D. Case 4: Large Network Size and Different Topologies

Tables IV-VI show the convergence performance comparison under various grid topologies, network sizes, and transmission rates. As shown in the figures, it is concluded that increas-

TABLE IV
CONVERGENCE PERFORMANCE OF THE PROPOSED ALGORITHM

Topology	$R_{\max}$ /Mbit/s	J=5		J=10	
		Convergence time /s	Convergence deviation /V	Convergence time /s	Convergence deviation /V
Complete Topology	15	0.43	0	0.59	0
	20	0.35	0	0.42	0
Ring Topology	15	0.68	0	1.09	0.02
	20	0.45	0	0.56	0
Bus Topology	15	0.67	0	1.2	0.01
	20	0.44	0	0.53	0
Star Topology	15	0.62	0	2.22	0.03
	20	0.42	0	0.49	0.02

TABLE V
CONVERGENCE PERFORMANCE OF BASELINE 1

Topology	$R_{\max}$ /Mbit/s	J=5		J=10	
		Convergence time /s	Convergence deviation /V	Convergence time /s	Convergence deviation /V
Complete Topology	15	0.59	0	Non-convergence	
	20	0.42	0	Non-convergence	
Ring Topology	15	0.63	0.01	Non-convergence	
	20	0.56	0	Non-convergence	
Bus Topology	15	0.66	0.01	Non-convergence	
	20	0.45	0	Non-convergence	
Star Topology	15	0.67	0.01	Non-convergence	
	20	0.46	0	Non-convergence	

TABLE VI
CONVERGENCE PERFORMANCE OF BASELINE 2

Topology	$R_{\max}$ /Mbit/s	J=5		J=10	
		Convergence time /s	Convergence deviation /V	Convergence time /s	Convergence deviation /V
Complete Topology	15	0.54	0.01	Non-convergence	
	20	0.38	0	Non-convergence	
Ring Topology	15	0.87	0	Non-convergence	
	20	0.55	0	Non-convergence	
Bus Topology	15	0.71	0	Non-convergence	
	20	0.58	0	0.79	0.01
Star Topology	15	0.70	0	Non-convergence	
	20	0.48	0	Non-convergence	

ing information interaction capability and transmission rates between nodes is beneficial for convergence improvement. However, both baseline algorithms show non-convergence under large network size $J = 10$. Even in smaller network with $J = 5$, they fail to reach the optimal convergence and a 0.01V voltage deviation is observed, e.g., baseline 1 at ring, bus, and star topologies with $R_{\max} = 15$ Mbit/s, and baseline 2 at ring topology with $R_{\max} = 15$ Mbit/s. Compared to baseline algorithms, the proposed algorithm always shows the smallest convergence time under different topologies, network sizes, and transmission rates, demonstrating great scalability, flexibility, and robustness. When the network size is increased from $J = 5$ to $J = 10$, the proposed algorithm maintains zero voltage deviation even in the topologies of ring, bus, and star with limited node interconnections.

VI. CONCLUSION

In this paper, the integrated optimization problem of sensing, transmission, computing, and control in power-communication coupling smart grid has been addressed. The formulated problem is solved in three stages by self-penalty DAC-based sensing-transmission collaborative optimization, computing resource allocation for optimal AoI, and control optimization based on AoTI. Simulation results of four cases validated the superior performance of the proposed algorithm in improving power-domain voltage stability. It is verified that the proposed algorithm has practical feasibility, scalability, and robustness under load fluctuation, grid topology variation, communication failure, large network size and different topologies. Compared to baseline 1 with conventional consensus and time-triggering mechanisms, the proposed algorithm increases the control convergence speed by 53.68%. Compared

to baseline 2, the convergence deviation is eliminated under large network size and different topologies, demonstrating the advantages of integrated optimization. Furthermore, compared to control algorithms based on communication delay and AoI, the proposed algorithm based on novel metric AoTI reduces convergence delay by 53.96% and 36.51%, respectively, and effectively resists FDI attacks.

In future work, we will focus on testbed development and investigate real-world implementation in smart grid. For testbed development, we will develop lightweight software based on docker and virtualization, and embedded hardware based on structure-function decoupling. The proposed algorithm will be packaged and implemented as a microservice. Next, real-world experiment under various typical grid test sites will be carried out, including rooftop photovoltaic and battery energy storage systems. The rules for parameter setting in different power grid scenarios will be investigated and established via real-world experiment. Last but not least, we will extend the study into the coupling among power, communication, and transportation domains. The influence of aggregated response characteristics of electric vehicles and the temporal-spatial distribution of traffic flows on joint resource allocation and consensus control will be analyzed.

REFERENCES

[1] H. Liao *et al.*, "Integration of 6G signal processing, communication, and computing based on information timeliness-aware digital twin," *IEEE J. Sel. Top. Signal Process.*, vol. 18, no. 1, pp. 98–108, Jan. 2024.

[2] T. Yang, S. Sun, and G. Liu, "Distributed discrete-time secondary cooperative control for AC microgrids with communication delays," *IEEE Trans. Ind. Electron.*, vol. 70, no. 6, pp. 5949–5959, Jun. 2023.

[3] D. Shi *et al.*, "Deception attack detection of isolated DC microgrids under consensus-based distributed voltage control architecture," *IEEE J. Emerging Sel. Topics Circuits Syst.*, vol. 11, no. 1, pp. 155–167, Mar. 2021.

[4] M. Hua *et al.*, "Integrated sensing and communication: Joint pilot and transmission design," *IEEE Trans. Wireless Commun.*, vol. 23, no. 11, pp. 16 017–16 032, Nov. 2024.

[5] C. Ding, J.-B. Wang, H. Zhang, M. Lin, and G. Y. Li, "Joint optimization of transmission and computation resources for satellite and high altitude platform assisted edge computing," *IEEE Trans. Wireless Commun.*, vol. 21, no. 2, pp. 1362–1377, Feb. 2022.

[6] X. Cai, Y. Fan, W. Yue, Y. Fu, and C. Li, "Dependency-aware task scheduling for vehicular networks enhanced by the integration of sensing, communication and computing," *IEEE Trans. Veh. Technol.*, vol. 73, no. 9, pp. 13 584–13 599, Sept. 2024.

[7] N. Huang *et al.*, "Mobile edge computing aided integrated sensing and communication with short-packet transmissions," *IEEE Trans. Wireless Commun.*, vol. 23, no. 7, pp. 7759–7774, Jul. 2024.

[8] Y. Yu, G.-P. Liu, and W. Hu, "Coordinated distributed predictive control for voltage regulation of DC microgrids with communication delays and data loss," *IEEE Trans. Smart Grid*, vol. 14, no. 3, pp. 1708–1722, May 2023.

[9] Y. Li, C. Lu, Y. Tang, C. Fang, and Y. Cui, "Dynamic control and time-delayed channel scheduling co-design for voltage control in active distribution networks," *IEEE Trans. Smart Grid*, vol. 15, no. 2, pp. 1837–1848, Mar. 2024.

[10] C. Peng and J. Zhang, "Delay-distribution-dependent load frequency control of power systems with probabilistic interval delays," *IEEE Trans. Power Syst.*, vol. 31, no. 4, pp. 3309–3317, July 2016.

[11] M. Shi *et al.*, "Distributed optimal control of energy storages in a DC microgrid with communication delay," *IEEE Trans. Smart Grid*, vol. 11, no. 3, pp. 2033–2042, May 2020.

[12] H. Liao *et al.*, "Ultra-low AoI digital twin-assisted resource allocation for multi-mode power IoT in distribution grid energy management," *IEEE J. Sel. Areas Commun.*, vol. 41, no. 10, pp. 3122–3132, Apr. 2023.

[13] X. Cao, J. Wang, Y. Cheng, and J. Jin, "Optimal sleep scheduling for energy-efficient AoI optimization in industrial internet of things," *IEEE Internet Things J.*, vol. 10, no. 11, pp. 9662–9674, Jun. 2023.

[14] Z. Jiang, B. Krishnamachari, X. Zheng, S. Zhou, and Z. Niu, "Timely status update in wireless uplinks: Analytical solutions with asymptotic optimality," *IEEE Internet Things J.*, vol. 6, no. 2, pp. 3885–3898, Apr. 2019.

[15] H. Liao *et al.*, "Information timeliness aware multispectral integrated sensing, communication, and computing for high-voltage discharge detection," *IEEE Trans. Commun.*, vol. 73, no. 1, pp. 245–258, Jan. 2025.

[16] X. Zheng, S. Zhou, and Z. Niu, "Urgency of information for context-aware timely status updates in remote control systems," *IEEE Trans. Wireless Commun.*, vol. 19, no. 11, pp. 7237–7250, Nov. 2020.

[17] M. Klügel, M. H. Mamduhi, S. Hirche, and W. Kellerer, "AoI-penalty minimization for networked control systems with packet loss," in *2019 IEEE INFOCOM*, Paris, France, 2019, pp. 189–196.

[18] J. Cao *et al.*, "Age of loop oriented wireless networked control system: Communication and control co-design in the FBL regime," in *2022 IEEE INFOCOM*, New York, USA, 2022, pp. 1–6.

[19] Z. Jiang *et al.*, "SMART: Situationally-aware multi-agent reinforcement learning-based transmissions," *IEEE Trans. Cognit. Commun. Networking*, vol. 7, no. 4, pp. 1430–1443, Dec. 2021.

[20] X.-K. Liu, S.-Q. Wang, M. Chi, Z.-W. Liu, and Y.-W. Wang, "Resilient secondary control and stability analysis for DC microgrids under mixed cyber attacks," *IEEE Trans. Ind. Electron.*, vol. 71, no. 2, pp. 1938–1947, 2024.

[21] Y. Wei, F. R. Yu, M. Song, and Z. Han, "User scheduling and resource allocation in HetNets with hybrid energy supply: An actor-critic reinforcement learning approach," *IEEE Trans. Wireless Commun.*, vol. 17, no. 1, pp. 680–692, Jan. 2018.

[22] K. Wang *et al.*, "Task offloading with multi-tier computing resources in next generation wireless networks," *IEEE J. Sel. Areas Commun.*, vol. 41, no. 2, pp. 306–319, Feb. 2023.

[23] M. Shi, M. Shahidehpour, Q. Zhou, X. Chen, and J. Wen, "Optimal consensus-based event-triggered control strategy for resilient DC microgrids," *IEEE Trans. Power Syst.*, vol. 36, no. 3, pp. 1807–1818, May 2021.

[24] M. Jamali, M. S. Sadabadi, M. Davari, S. Sahoo, and F. Blaabjerg, "Resilient cooperative secondary control of islanded AC microgrids utilizing inverter-based resources against state-dependent false data injection attacks," *IEEE Trans. Ind. Electron.*, vol. 71, no. 5, pp. 4719–4730, May 2024.

[25] M. Shi *et al.*, "Distributed optimal control of energy storages in a DC microgrid with communication delay," *IEEE Trans. Smart Grid*, vol. 11, no. 3, pp. 2033–2042, May 2020.

Haijun Liao (Member, IEEE) received the B.Eng. degree in smart grid information engineering in 2019 and received the Ph.D. degree in electrical engineering in 2024 from North China Electric Power University, Beijing, China. She is currently an assistant professor with North China Electric Power University. Her research interest includes power internet of things, cyber-physical systems, cloud-edge-end collaboration, sensing-transmission-computing-control integration. She was the recipient of the IEEE IWCMC 2019 Best Paper Award, IEEE VTC-2020 Spring Best Student Paper Award, and IEEE CAMAD 2021 Best Paper Award.

Hongxu Yan is currently working toward the B.E. degree in communication engineering from North China Electric Power University, Beijing, China. His research interests include resource allocation and network security in smart grid communication and power internet of things.

Wen Zhou received the B.E. degree in electronic information engineering in 2024 from North China Electric Power University, Beijing, China, where he is currently working toward the M.Eng degree. His research interests include resource allocation and network security in smart grid communication and power internet of things.

Wenxuan Che received the B.Eng. degree in communication engineering in 2024 from North China Electric Power University, Beijing, China. She is currently working toward the M.Eng. degree in information and communication engineering with the School of Electrical and Electronic Engineering, North China Electric Power University, Beijing, China. Her research interests include power internet of things and resource allocation optimization of power communication network.

Haodong Liu received the B.E. degree in communication engineering in 2023 from North China Electric Power University, Beijing, China, where he is currently working toward the M.Eng degree. His research interests include resource allocation in smart grid communication and power internet of things.

Zhenyu Zhou (Senior Member, IEEE) received the M.E. and Ph.D. degrees in international information and communication studies from Waseda University, Tokyo, Japan, in 2008 and 2011, respectively. From September 2012 to April 2019, he was an Associate Professor with the School of Electrical and Electronic Engineering, North China Electric Power University, Beijing, China, where he has been a Full Professor since April 2019. His research interests include power internet of things, smart grid information and communication, sensing-transmission-computing-control integration, and smart grid energy management. He was the recipient of the IET Premium Award in 2017, IEEE Globecom 2018 Best Paper ward, IEEE International Wireless Communications and Mobile Computing Conference 2019 Best Paper Award, and IEEE Communications Society Asia Pacific Board Outstanding Young Researcher. He was an Associate Editor for IEEE Internet of Things Journal, IET Quantum Communication, IEEE Access, EURASIP Journal on Wireless Communications and Networking, and Transactions on Emerging Telecommunications Technologies, and the Guest Editor of IEEE Communications Magazine and IEEE Transactions on Industrial Informatics. He is an IET Fellow and a Senior Member of the Chinese Institute of Electronics and the China Institute of Communications.

Shahid Mumtaz (Senior Member, IEEE) received the M.Sc. degree in electrical and electronic engineering from the Blekinge Institute of Technology, Karlskrona, Sweden, in 2006, and the Ph.D. degree in electrical and electronic engineering from the University of Aveiro, Portugal, in 2011. He has over seven years of wireless industry experience. He was a Research Intern with Ericsson, Karlskrona, and Huawei Research Labs, Karlskrona, in 2005. He is currently a Senior Research Scientist and a Technical Manager with the Instituto de Telecomunicações Aveiro, Portugal. His M.Sc. and Ph.D. degrees were funded by the Swedish Government and FCT Portugal. He has been involved in several EC Research and Development Projects (5GPP-Speed-5G, CoDIV, FUTON, C2POWER, GREENET, GREEN-T, ORCALE, ROMEO, FP6, and FP7) in the field of green communication and next generation wireless systems. In the EC projects, he holds the position of Technical Manager, where he oversees the project from a scientific and technical side, managing all details of each work packages, which gives the maximum impact of the projects results for the further development of commercial solutions. He has over 90 publications in international conferences, journal papers, and book chapters. He has served on the technical program committees of different IEEE conferences, including Globecom, ICC, and VTC, and chaired some of their symposia. He has served as the workshop chair of many conferences and was a recipient of the 2006 IITA Scholarship, South Korea. He is serving as the Vice-Chair of the IEEE 5G Standardization. He is also an Editor of three books and served as a Guest Editor for a special issue of the IEEE Wireless Communications Magazine and the IEEE Communication Magazine. He was recently appointed a permanent Associate Technical Editor of the IEEE Communication Magazine, the IEEE Journal of IoT, and the Journal of Digital Communication and Network (Elsevier).